Comparison of the experimental response of two horizontal axis tidal turbines to wave and current from a frequency dependency point of view

Marc-amaury Dufour, Grégory Pinon, Benoît Gaurier, Grégory Germain, Jean-Valéry Facq, Michael Togneri, Fabio Represas, Erwann Nicolas, Julie Marcille

Comparison of the experimental response of two horizontal axis tidal turbines to wave and current from a frequency dependency point of view

M.-A. Dufour & G. Pinon
Normandie Univ, UNILEHAVRE, UMR 6294 CNRS, LOMC 76600 Le Havre, France

B. Gaurier & G. Germain & J.-V. Facq
IFREMER, Marine Structure Laboratory, 150 quai Gambetta, BP 699, 62321 Boulogne-sur-mer, France

M. Togneri
Energy & Environment Research Group, Swansea University, Bay Campus, Swansea SA1 8EN, UK

F. Represas
Magallanes Renovables, Prego de Montaos 7, Redondela, 36800, Spain

E. Nicolas & J. Marcille
Sabella S.A., 7 Rue Felix Le Dantec, 29000 Quimper, France

ABSTRACT: This paper studies wave influence on two horizontal axis tidal turbines developed by industrial partners: Sabella and Magallanes Renovables. The trials are performed in a wave and current flume tank where upstream flow conditions are monitored thanks to Laser Doppler Velocimetry. Wave amplitude and orbital amplitude are computed thanks to least mean square method. The turbulence is analysed through its intensity and a power spectral density point of view. A special attention is paid to turbine immersion depth. Global torque and thrust are analyzed in the frequency domain thanks to power spectral density and magnitude square coherence. Wave generates a strong torque and thrust fluctuation level of the same order as the mean effort level. Both torque and thrust respond to wave at wave and twice the wave frequency for all turbines whatever the immersion.

1 INTRODUCTION

Tidal Energy Converters (TEC) experience harsh conditions, including strong upstream flows such as the ones encountered in the Alderney Race. In this highly energetic area, the turbulence intensity is about 6 % to 13 % (Thiébaut et al. 2020), and wave can reach a significant height of 7 m and a peak period of 13 s during the Eleanor storm (Furgerot et al. 2020) for instance.

The MONITOR project was launched in 2018 (Togneri et al. 2019). The main objective of this project is to improve the TEC reliability facing those severe real-life conditions. This program is supported by the Interreg Atlantic Area because the Atlantic region in western Europe presents one of the biggest tidal potential in the world. Through multiple testing techniques: in-situ measurements, numerical simulations, and flume tank trials, the MONITOR project aims at better understanding TEC response to such conditions. Based upon former studies evaluating TEC blade loads variations due to turbulence (Medina et al. 2017, Blackmore et al. 2016), experimental testings carried out during the MONITOR project enabled TEC response to turbulence (Slama et al. 2021) to be quantified. The results show that loads standard deviation at peak performance Tip Speed Ratio, i.e. nominal TSR, are three times higher in high turbulence cases versus low turbulence cases. Moreover, depending on TEC design, turbulence may affect the overall turbine performance of a few percent.

The present work, as part of flume tank testings of the MONITOR project, investigates TEC response to combined wave and turbulence effects. Previous studies (Galloway et al. 2014, Guo et al. 2018) have investigated the TEC response to wave exposure. All studies agree that torque and thrust standard deviation drastically increase in wave cases, with an amplitude depending on wave parameters, turbine im-

mersion and TSR. Nevertheless, wave effect on loads from a frequency dependency point of view is still unclear. The aim of the present work is to quantify the changes in the frequency domain due to wave. It also aims at completing the work presented in (Dufour et al. 2022) in which performance and blade root loads analysis highlight higher fluctuations when the turbine is close to the free surface.

This experimental study focuses on two pre-commercial devices from industrial partners of the MONITOR project: First, the Magallanes Renovables ATIR, a 2 MW device composed of a floating platform supporting two variable-pitch 3-bladed turbines ; secondly, the Sabella D12 bottom-mounted fixed-pitch and 5-bladed 1 MW device.

First, the experimental set-up and the upstream flow conditions are presented in section 2. The turbulence is analyzed thoroughly in section 3. Secondly, the effect of wave and immersion depth on torque Q, thrust T and blade root loads are analyzed from a frequency dependency point of view in section 4.

2 EXPERIMENTAL SET-UP AND UPSTREAM FLOW CONDITIONS

As the present work is a continuation of (Slama et al. 2021), the set-up description is very close to the one previously offered.

2.1 *Experimental set-up*

The trials are carried out in the IFREMER wave and current flume tank in Boulogne-sur-Mer. The flume tank working section is 18 m long, 4 m wide and $H =$ 2 m deep. The upstream flow velocity ranges from 0.1 to 2.2 m/s. The experimental set-up, illustrated in fig. 1, is the same for both turbines. The hub of the scaled turbine is set at a depth of either $z_0 =$ -1.0 m or $z_0 =$ -0.6 m below the free surface. The flow conditions are monitored at the hub center axis, approximately two turbine diameters upstream of the turbine, with a bi-component Laser Doppler Velocimeter (LDV). In order to monitor the quality of the LDV data, settings are tuned so that the validation parameter approaches 100 %.

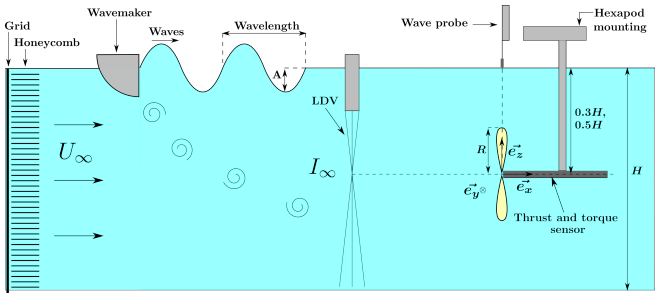

Figure 1: Schematic side view of the test configuration with turbine immersion being either $0.3H$ or $0.5H$.

Both the Magallanes Renovables ATIR and the Sabella D12 scaled models, shown in fig. 2, are based on the existing IFREMER mechanical and electrical generic turbine, a 3-bladed horizontal axis turbine. More details about the flume tank, the instrumentation and the IFREMER generic turbine can be found in (Slama et al. 2021, Gaurier et al. 2019). It is a fixed pitch device. This results in a major difference for the ATIR turbine. Whereas the full scale model has variable-pitch blades, the scaled model has fixed-pitch blades. Hence the ATIR blades will not be at the optimum pitch angle in all operating conditions. Model parameters are detailed in Table 1. ATIR and D12 blade profiles are confidential.

Table 1: Turbine model parameter description.

Description	ATIR	D12
Rotor Radius R [mm]	338	300
Hub Radius [mm]	55	96
Number of blades	3	5

The scale of the ATIR and the D12 models are 1:28 and 1:20 respectively. The Froude criterion was preferred to the Reynolds criterion to scale the experimental set-up so as to ensure the wave similarity between the full and the model scale. Moreover the full scale Reynolds numbers are around 10^7 and these values cannot be obtained in the flume tank. The Froude scaling is detailed in (Slama et al. 2021). In this study, the Tip Speed Ratio (TSR) varies from 0 to 8 for both turbine. The torque and thrust are directly measured on the rotation axis while each blade root is equipped with a load-cell measuring two forces and three moments, see (Gaurier et al. 2019). Adapting the unconventional 5-bladed D12 to the IFREMER device forced to mount one blade alone, and the four other blades by groups of two. Finally, during all the trials, the turbine parameters and the flow velocity are recorded synchronously. The signals are sampled at a frequency of 128 Hz, excepted for the LDV which has an irregular sampling rate. The acquisition time is set to 180 s for all cases. Two cases are presented in this paper: "WM only" represents the case where the wavemaker is idle into the water, that is to say with current only. This case is mandatory to characterize the turbulence generated by the presence of the wavemaker. It is considered as the reference case. "A95-F05" represents the wave and current case, with a required wave amplitude of 95 mm (with no current) and wave frequency of 0.5 Hz.

2.2 *Upstream velocity conditions*

The upstream velocity along x-axis at the hub center z-position is defined by eq.(1) in agreement with the axis system presented in fig. 1.

$$u(t) = \overline{u} + u'(t) + u_{wave}(t), \quad (1)$$

where $\overline{u}$ is the temporal mean, $u'(t)$ is the fluctuating component due to turbulence and $u_{wave}(t)$ is the

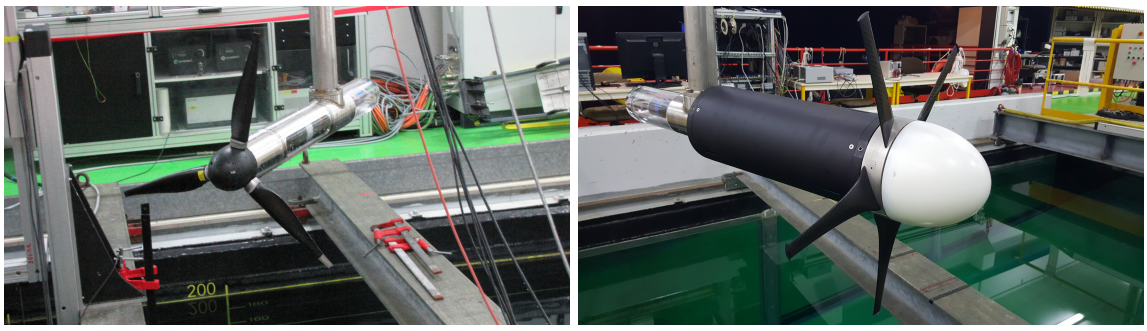

Figure 2: Pictures of the scaled models: left is Magallanes Renovables' ATIR, right is Sabella's D12.

orbital velocity component along x-axis. If there is no wave, $u_{wave}(t) = 0$. The required mean upstream axial velocity in these trials is $\overline{u} = 0.80$ m/s and measured values are summarized in Table 2.

2.3 *Wave major characteristics*

Wave is also experimentally studied. A wave probe records free surface elevation at the turbine x-position, see fig. 1 scheme. The measured wave amplitude comes from the wave probe signal processed with an in-house sinusoidal least mean square (LMS) code built according to (Jacquelin 2014). Measured wave amplitude in the flume tank is of 57 mm. The discrepancy with the required 95 mm without current is not only due to the current effect but also due to wavemaker transfer function and flume tank reflection. Moreover higher wave orders are not taken into account. The wave orbital velocity along x-axis is defined by $u_{wave}(t) = b\sin(\omega_{wave}t) + c\cos(\omega_{wave}t)$ with $b, c \in \mathbb{R}$ also evaluated thanks to the same LMS method computed on the LDV signal. Then wave orbital amplitude equates $\sqrt{b^2 + c^2}$. Wave parameters are detailed in Table 2.

Table 2: Waves parameters and mean upstream velocity.

Depth	Turbine	Wave	$\overline{u}$	Waves amplitude	Orbitals amplitude
m	-	-	m·s^{-1}	mm	m·s^{-1}
-1.0	ATIR	WM only	0.8	-	-
		A95-F05	0.81	57	0.08
	D12	WM only	0.79	-	-
		A95-F05	0.81	57	0.08
-0.6	ATIR	WM only	0.72	-	-
		A95-F05	0.7	57	0.11
	D12	WM only	0.72	-	-
		A95-F05	0.71	57	0.11

3 UPSTREAM TURBULENCE CHARACTERISTICS

3.1 *Turbulence intensity*

The incoming turbulence is at first regulated using flow straighteners, grid and honeycomb, placed at the inlet of the working section. Then the wavemaker presence generates turbulent structures that penetrate the water column. The ambient turbulence intensity in the flume tank is thus defined downstream of the wavemaker, at the LDV x-position, as presented in fig. 1. Each turbulence intensity is computed with the contribution of turbulence only: $u'(t)$, $v'(t)$ and $w'(t)$. That is to say the first order wave contribution is removed from the velocity signal for u and w components when needed. According to (Blackmore et al. 2016, Medina et al. 2017), the 1D turbulence intensity can be defined by:

$$I_{1D} = \frac{\sigma_{u'}}{\overline{u}} \tag{2}$$

The 3D turbulence intensity is defined by eq. (3). An isotropy assumption between the v' and w' components is made. This signifies that for both of them, mean and standard deviation are of the same order of magnitude. This hypothesis has been verified thanks to velocity profiles measured with a tri-component LDV after the turbine models trials. The obtained I_{3D} at each depth state that the isotropy hypothesis is true for $z <$ -0.3 m. Then, as the turbine hub is at $z_0 =$ -0.6 m or $z_0 =$ -1.0 m, this hypothesis is valid for the studied domain. The isotropy hypothesis between the v' and w' components enables the 3D turbulence intensity to be computed using the data from the bi-component LDV.

$$I_{3D} = \sqrt{\frac{1/3(\sigma_{u'}^2 + \sigma_{v'}^2 + \sigma_{w'}^2)}{\overline{u}^2 + \overline{v}^2 + \overline{w}^2}}$$

$$\simeq \sqrt{\frac{1/3(\sigma_{u'}^2 + 2\sigma_{v'}^2)}{\overline{u}^2 + 2\overline{v}^2}} \simeq \sqrt{\frac{1/3(\sigma_{u'}^2 + 2\sigma_{w'}^2)}{\overline{u}^2 + 2\overline{w}^2}} \tag{3}$$

The different turbulence intensities from eq. (2) and eq. (3) are presented in Table 3. The wavemaker presence generates an ambient turbulence intensity from $I_{3D} \approx 10\%$ to $I_{3D} \approx 15\%$ depending on depth in water column. Thus, this I_{3D} range corresponds to measured in-situ values (Thiébaut et al. 2020). Insofar as the turbulence intensity does not provide any clue on the spatial characteristics of the turbulence, some important turbulence length scales have to also be studied according to (Slama et al. 2021).

3.2 *Integral length scale*

The integral length scale represents the dimension of the most energetic eddies. The resulting values are

presented in Table 3. The autocorrelation coefficient of the turbulent part of the velocity u' is computed. With a discrete velocity signal, the time delay τ_n is defined by $\tau_n = n/f_s$, where f_s is the sampling frequency and $n \in \mathbb{N}$. $\tau_N = N/f_s$, $N \in \mathbb{N}$, is the maximum time delay on which the autocorrelation coefficient is computed. Then, the autocorrelation coefficient is defined as in eq. (4). An example is shown in fig. 3 for the "WM only" case on Sabella D12 turbine model at z_0 = -1.0 m. The autocorrelation is computed for each run of the case and then the mean is kept as the autocorrelation curve for the given case.

$$R(\tau_n) = \frac{1}{N\sigma_{u'}^2} \sum_{k=0}^{N-1} u'(\tau_k)u'(\tau_{k+n}) \tag{4}$$

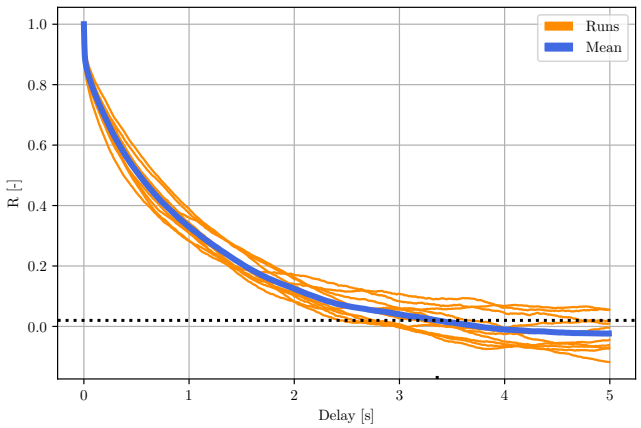

Figure 3: $R(\tau_n)$ for Sabella D12 in "WM only" at z_0 = -1.0 m.

The integral time scale T is then calculated by integrating the autocorrelation coefficient from 0 until the first delay, named $\tau_0 = M/f_s$, where the autocorrelation coefficient crosses the y-axis 0 value. In practice, a threshold close to 0, shown in fig. 3, is chosen to ensure 0-crossing, as in (Blackmore et al. 2016). The trapezoidal rule is used to compute the discrete integration. This leads to T definition in eq. (5).

$$T = \sum_{k=1}^{M-1} \frac{\tau_{k+1} - \tau_k}{2} \Big(R(\tau_{k+1}) + R(\tau_k) \Big) \tag{5}$$

Eventually, thanks to Taylor's frozen eddy hypothesis, the integral length scale L, can be defined by eq. (6).

$$L = \overline{u}T \tag{6}$$

3.3 *Signal processing hypothesis*

Studied signals are assumed to be weak sense stationary stochastic processes. It means that their mean and autocorrelation are equals whenever they are computed, see (Pishro-Nik 2014). Signals are assumed to be of zero mean. For instance, on the velocity, computations are done on $u_{wave}(t) + u'(t)$, eq. (1). The Power Spectral Densities (PSD) are computed with an in-house algorithm based upon (Welch 1967), and (Cooley and Tukey 1965) for the Fast Fourier Transform part. The PSD of a physical quantity A is noted S_{AA}. The velocity signal is evenly sampled with linear interpolation at a time step corresponding to the average of all the uneven time steps. The Magnitude Square Coherences (MSC) are computed with an in-house code based upon (Carter, Knapp, & Nuttall 1973, Cooley & Tukey 1965). The MSC between two physical quantities B and C is noted γ_{BC}^2.

3.4 *Turbulence length scales and spectral analysis*

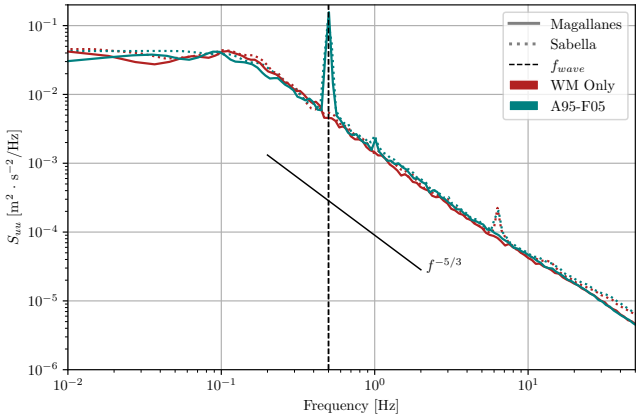

Figure 4: Velocity PSD, S_{uu} at -0.6 m.

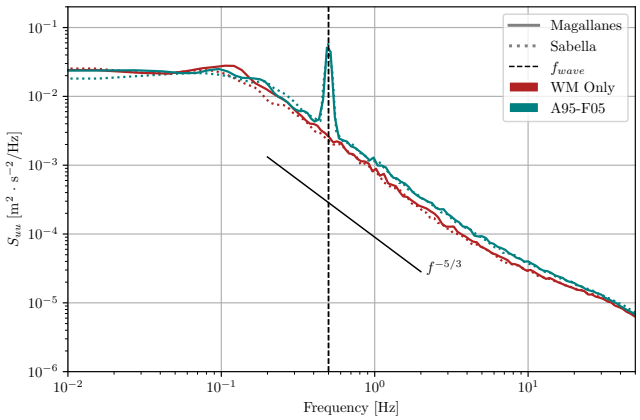

Figure 5: Velocity PSD, S_{uu} at -1.0 m.

The longest the sample is, the better the result will be. Thus, in fig. 4 and fig. 5, the PSD are computed on all the runs, one run per TSR. The striking elements from fig. 4 and fig. 5 are listed below:

- For the "A95-F05" case, the wave generated spike is precisely on the wave frequency 0.5 Hz ;
- Below the level 10^{-4} m^2 · s^{-2}/Hz, a change of slope is noticed. This change is of lower magnitude at z_0 = -0.6 m compared to z_0 = -1.0 m. It is the result of noise measurement due to LDV settings not accurately tuned because the optic fibre was partly corrupt. Thus this point hides the real upper frequency of the inertial subrange ;

Table 3: Turbulence intensities, integral length scale L, dissipation rate ε and spatial characteristics of the inertial subrange.

Depth	Turbine	Wave	I_{1D}	I_{3D}	L	ε	l	η	λ	Re_λ
m	-	-	%	%	m	$m^2 \cdot s^{-3}$	m	m	m	-
-1.0	ATIR	WM only	11.9	10.1	0.6	1.6×10^{-3}	0.54	2×10^{-4}	1×10^{-2}	8.2×10^2
		A95-F05	12.1	10.8	0.53	2.4×10^{-3}	0.39	2×10^{-4}	8×10^{-3}	7.1×10^2
	D12	WM only	11.2	9.3	0.67	1.4×10^{-3}	0.49	2×10^{-4}	1×10^{-2}	7.6×10^2
		A95-F05	12.1	10.3	0.47	2.4×10^{-3}	0.38	2×10^{-4}	8×10^{-3}	7.0×10^2
-0.6	ATIR	WM only	17.2	14.8	0.51	4.2×10^{-3}	0.45	1×10^{-4}	8×10^{-3}	8.5×10^2
		A95-F05	17.5	15.7	0.48	5.0×10^{-3}	0.37	1×10^{-4}	7×10^{-3}	7.7×10^2
	D12	WM only	17.5	15.4	0.52	4.7×10^{-3}	0.43	1×10^{-4}	8×10^{-3}	8.4×10^2
		A95-F05	17.9	16.3	0.5	5.8×10^{-3}	0.35	1×10^{-4}	7×10^{-3}	7.6×10^2

- On Sabella cases at -0.6 m, the spike at 6.5 Hz results from vibrations of the LDV structure. When they have been noticed, fairings decreasing those vibrations were mounted on the LDV. Then this spike is not present for the other cases ;
- The inertial subrange PSD slope β is very close to $5/3 = 1.667$.

It is assumed that the velocity PSD, $S_{uu}(f)$, can be described by eq. (7) in the inertial subrange.

$$S_{uu}(f) = C_0 f^{-\beta}, \tag{7}$$

with C_0 the intercept and β the slope of the logarithmic straight line.

For each case $\beta \in [1.58, 1.74]$. This confirms that the inertial subrange PSD slope is very close to the $5/3$ theoretical value. They are computed with the in-house linear LMS method. This computation is done on the logarithm of the PSD, deprived of the wave generated spike seen in fig. 4 and fig. 5. The choice of the frequency range of the inertial subrange has a strong effect on the C_0 and β results. According to Kolmogorov's -5/3 law, presented in (Tennekes and Lumley 1972), the velocity PSD in the inertial subrange is described with the theoretical formula from eq. (8).

$$S_{uu}(k) = C\varepsilon^{2/3} k^{-5/3}, \tag{8}$$

where $C \simeq 1.5$ is the universal Kolmogorov constant, and ε is the turbulence dissipation rate.

According to Taylor's frozen eddy hypothesis the wavenumber k is related to the frequency by $k = 2\pi f/\overline{u}$. As $S_{uu}(f)$ is dimensionally homogeneous to $S_{uu}(k)/\overline{u}$, eq. (8) becomes eq. (9) in the frequency domain.

$$S_{uu}(f) = C\varepsilon^{2/3} \frac{\overline{u}^{2/3}}{(2\pi)^{5/3}} f^{-5/3} \tag{9}$$

When the slope β obtained is close enough to $5/3$, the dissipation rate can be estimated combining eq. (7) and eq. (9). Eq. (9) differs from previous studies. So the results presented in Table 3 for ε and the resulting length scales will also differ. According to (Tennekes and Lumley 1972, Blackmore et al. 2016), other turbulent length scales needs to be characterized. The previously determined turbulence dissipation rate ε, assuming kinematic viscosity of water is $\nu \approx 1.141\ 10^{-6}\ m^2/s$, enable the injection scale l, Kolmogorov's dissipation scale η, and Taylor length scale λ and Reynolds number Re_λ, to be computed. Those length scales, presented in Table 3, enable the spatial characteristics of the turbulence to be better understood. In particular, it will help to reproduce the flow characteristics numerically in further works.

According to Table 3, wavemaker movements seem to have different effects depending on the turbulence characteristic under scrutiny. First, the size of the most energetic eddies, the integral length scale L, is very close whether there is wave or not. A small effect of the immersion depth is noticed. While the average L at z_0 = -1.0 m is $L = 0.6$ m ; it is $L = 0.5$ m at z_0 = -0.6 m. This spatial inhomogeneity is coherent with the experimental set-up, fig. 1. As the wavemaker generates the turbulence, it is more likely not to have the same spatial characteristics in the water column. At each depth, for each turbine, when the wavemaker is active, the dissipation rate ε increases of 1 $m^2 \cdot s^{-3}$. An effect of the immersion depth is also noticed on the turbulence dissipation rate. For a given turbine and case, "A95-F05" or "WM only", going from z_0 = -1.0 m to z_0 = -0.6 m doubles the dissipation rate magnitude. Eventually, the difference in dissipation rate between "A95-F05" (wavemaker moving) or "WM only" (wavemaker only idle into the water), is also visible on the injection length scale l. This is not visible on the Kolmogorov's dissipation scale or the Taylor length scale inasmuch as their definition is less dependent on ε variations.

4 TORQUE AND THRUST SPECTRAL ANALYSIS

Signals hypothesis have been described in section 3.3. While a MSC close to zero 0 denotes that the two physical quantities are not correlated, a MSC higher than 0.6, arbitrary threshold, highlights strong correlation. When computing the MSC of the even sampled velocity with another signal, they are both resampled at the biggest time step between the two with linear interpolation. X-axis of all the PSD and MSC presented in this section 4 are normalized by the rotation frequency $f_0 = f_{rot}$ in order to improve readability and comparison between different TSRs.

4.1 *ATIR loads spectral analysis*

Magallanes Renovables ATIR spectral analysis is computed for peak performance $TSR = 6.7$ at depth -0.6 m and $TSR = 6.0$ at depth -1.0 m.

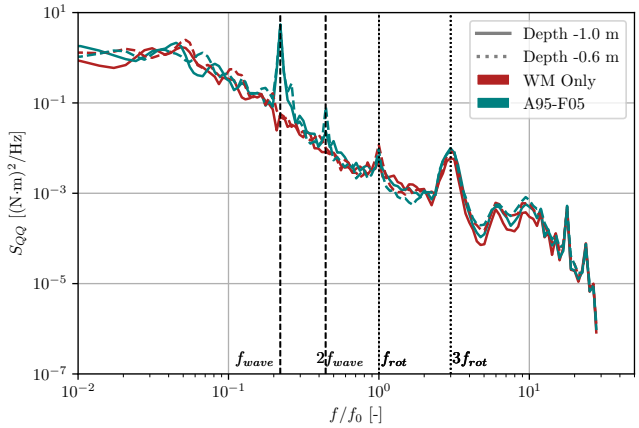

Figure 6: ATIR torque PSD S_{QQ}.

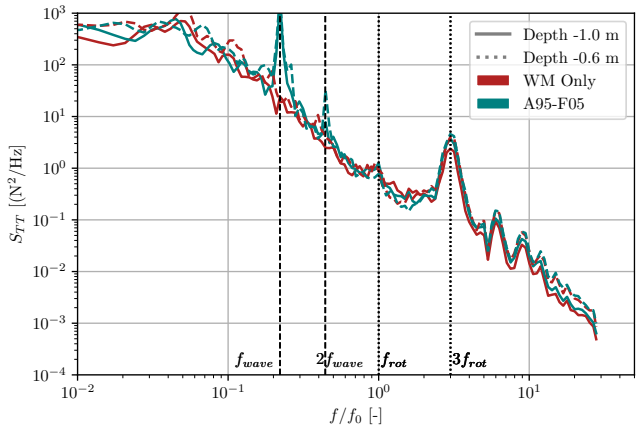

Figure 7: ATIR thrust PSD S_{TT}.

The torque Q and thrust T power spectral densities are presented on fig. 6 and fig. 7. Both Q and T are wave sensitive with a power density of the same level for both immersion -0.6 m and -1.0 m at the wave frequency. The second harmonic of the wave frequency is also noticed in both load PSD spectrum. While Q is sensitive to both the rotation frequency and the third harmonic of the rotation frequency at an equivalent power density level, the thrust T responds only to the third harmonic of the rotation frequency. This third harmonic corresponds to the number of blades of the Magallanes Renovables turbine.

The torque Q and thrust T coherences with the upstream velocity u are presented on fig. 8 and fig. 9. At low frequency, the high level MSC denotes a strong correlation between T and u and also between Q and u. With a threshold fixed at 0.6, a cut-out frequency around $0.15 f_{rot}$ appears. Then at high frequency there is no coherence at all between either Q or T and u. In spite of the cut-out frequency at $0.15 f_{rot}$, a spike on the wave frequency is observable for both γ^2_{uQ} and γ^2_{uT} which denotes for both Q and T a strong sensitivity to wave orbitals, as previously seen in the PSD analysis.

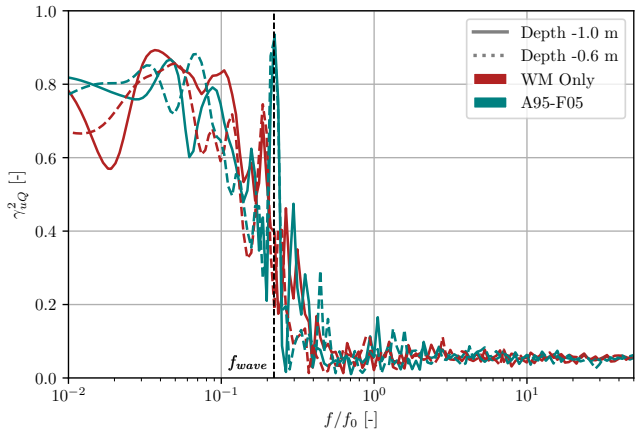

Figure 8: ATIR torque and inflow velocity MSC γ^2_{uQ}.

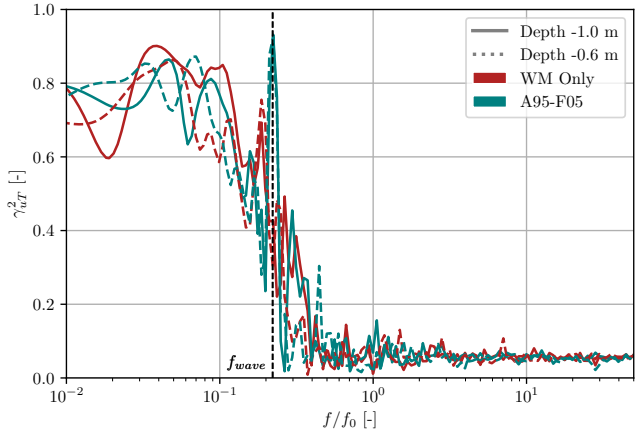

Figure 9: ATIR thrust and inflow velocity MSC γ^2_{uT}.

The torque Q and thrust T coherences with the rotational velocity ω are presented on fig. 10 and fig. 11. Firstly, an effect of the immersion depth is observable on the coherences with the rotational velocity. While at -1.0 m both $\gamma^2_{\omega Q}$ and $\gamma^2_{\omega T}$ goes below 0.4 at low frequency, which means there is no strong coherence anymore ; at -0.6 m the coherence remains high at low frequency. At -1.0 m the cut-in frequency appears to be around $0.03 f_{rot}$. For both immersion depth, both $\gamma^2_{\omega Q}$ and $\gamma^2_{\omega T}$ goes to 1.0 at the wave frequency. However, it is interesting to notice here another effect of the immersion depth. At -1.0 m, an extinction of the coherence just in front of the wave frequency is no-

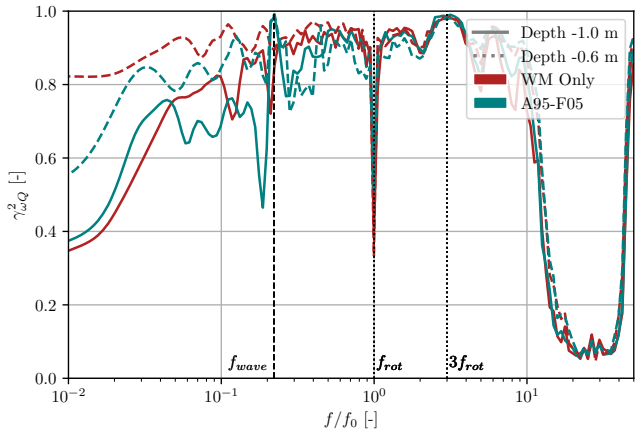

Figure 10: ATIR torque and rotational velocity MSC $\gamma^2_{\omega Q}$.

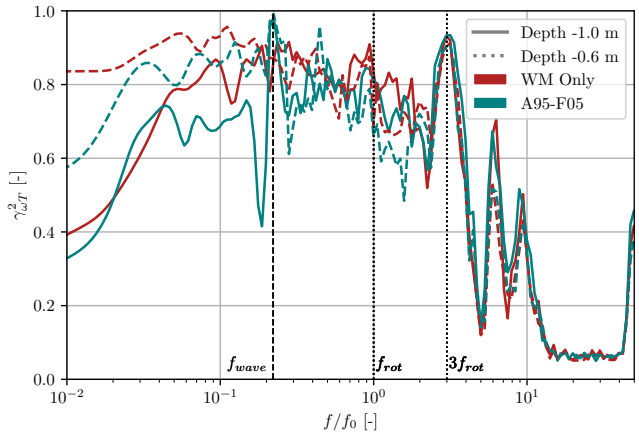

Figure 11: ATIR thrust and rotational velocity MSC $\gamma^2_{\omega T}$.

ticeable. Both $\gamma^2_{\omega Q}$ and $\gamma^2_{\omega T}$ are very high for the third harmonic of f_{rot} which corresponds to the blade number. Moreover it strengthens the results of the PSD from fig. 6 and fig. 7. The cut-out frequency is about $7f_{rot}$ for $\gamma^2_{\omega T}$ and about $15f_{rot}$ for $\gamma^2_{\omega Q}$. Thus this highlights that the torque is more sensitive to the rotational velocity high frequency variations than the thrust. A striking element is the extinction of $\gamma^2_{\omega Q}$ at f_{rot}. This effect was also reported in (Slama et al. 2021). The reasons behind this phenomenon are still unclear insofar as the torque is physically linked to the rotational velocity ω. This will be studied in future work thanks to trials performed on stiffness variations of the command control of the turbine model.

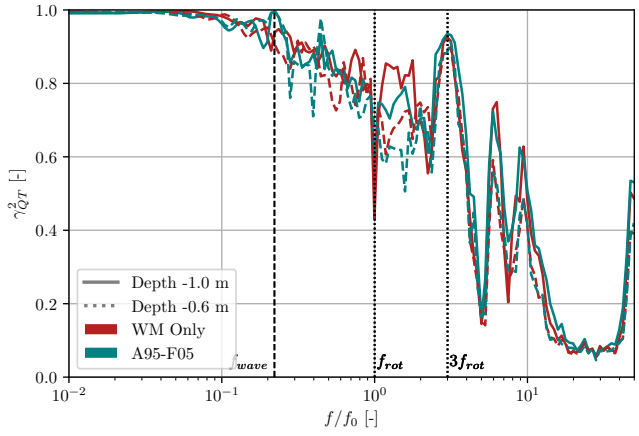

Figure 12: ATIR thrust and rotational velocity MSC γ^2_{QT}.

The coherence between torque Q and thrust T is very high until a cut-out frequency of about $10f_{rot}$ so nearly the whole range of frequencies under scrutiny. The wave effect is hidden by the very high coherence at low frequency. Eventually Q and T are highly correlated at the third harmonic of the rotation frequency.

4.2 *D12 loads spectral analysis*

Sabella D12 spectral analysis is performed at peak performance $TSR = 5.1$ at depth -0.6 m and $TSR = 4.5$ at depth -1.0 m.

The torque Q and thrust T power spectral densities are presented on fig. 13 and fig. 14. Both Q and T

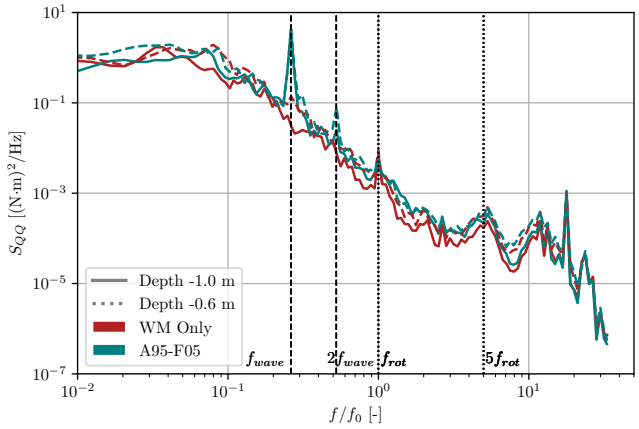

Figure 13: D12 torque PSD S_{QQ}.

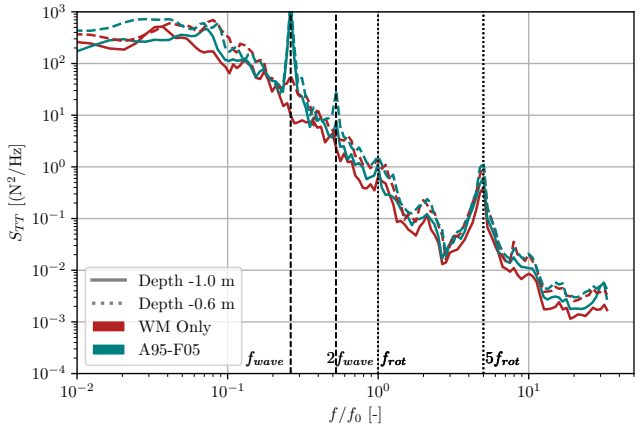

Figure 14: D12 thrust PSD S_{TT}.

are wave sensitive with a power density of the same level for both immersion -0.6 m and -1.0 m at the wave frequency. The second harmonic of the wave frequency is also noticed on both PSD spectrum. Both Q and T are sensitive to the rotation frequency and the fifth harmonic of the rotation frequency. This fifth harmonic corresponds to the number of blades of the Sabella turbine. However, the thrust T appears to be relatively more sensitive than the torque Q at the fifth harmonic of the rotation frequency. Eventually a little response of the thrust T at the second harmonic of the rotation frequency is noticed. This may be due to the 4 blades grouped by two. This mounting configuration can led to such a $2f_{rot}$ frequency appearance in the thrust PSD.

The torque Q and thrust T coherences with the upstream velocity u are depicted on fig. 15 and fig. 16. At low frequency, the high level of the MSC denotes a strong correlation between T and u and also between Q and u. With a threshold at 0.6, a cut-out frequency around $0.2f_{rot}$ appears. Then at high frequency there is no coherence at all between either Q or T and u. In spite of the cut-out frequency at $0.2f_{rot}$, a spike on the wave frequency is observable for both γ^2_{uQ} and γ^2_{uT} which denotes for both Q and T a strong sensitivity to wave orbitals.

The torque Q and thrust T coherences with the rotational velocity ω are presented on fig. 17 and fig. 18. Concerning the coherences with the rotational veloc-

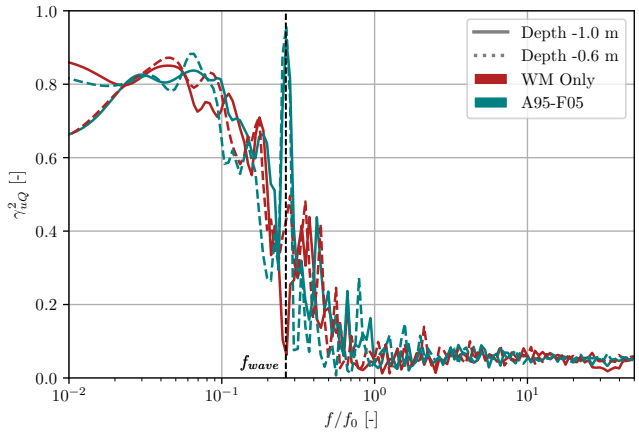

Figure 15: D12 torque and inflow velocity MSC γ^2_{uQ}.

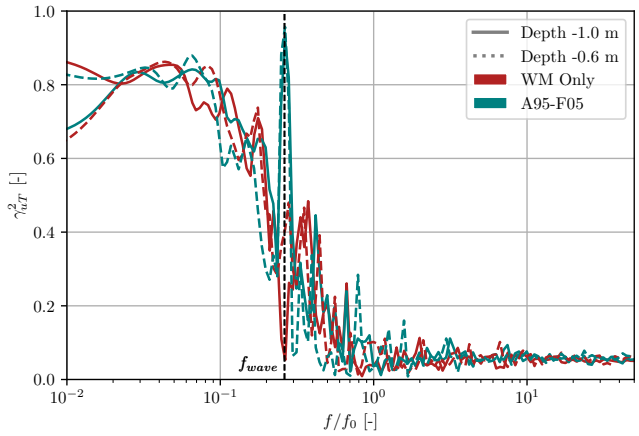

Figure 16: D12 thrust and inflow velocity MSC γ^2_{uT}.

ity, the effect of the immersion depth is even more noticeable here than the one noticed for the Magallanes Renovables turbine. While at -1.0 m both $\gamma^2_{\omega Q}$ and $\gamma^2_{\omega T}$ goes close to 0 at very low frequency, which means there no coherence at all ; at -0.6 m the coherence remains high, even at low frequency. At -1.0 m the cut-in frequency appears to be around $0.03 f_{rot}$ for the A95-F05 wave case and around $0.15 f_{rot}$ for the WM only case. For both immersion depth, both $\gamma^2_{\omega Q}$ and $\gamma^2_{\omega T}$ goes to 1.0 at the wave frequency. However, it is interesting to notice here another effect of the immersion depth and opposed to the one noticed for Magallanes this time. At -0.6 m, an extinction of

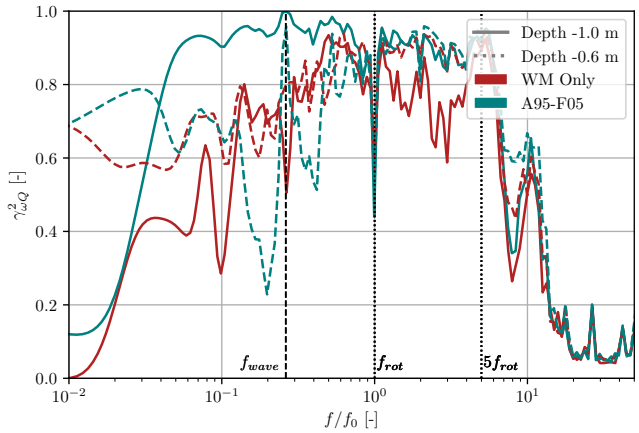

Figure 17: D12 torque and rotational velocity MSC $\gamma^2_{\omega Q}$.

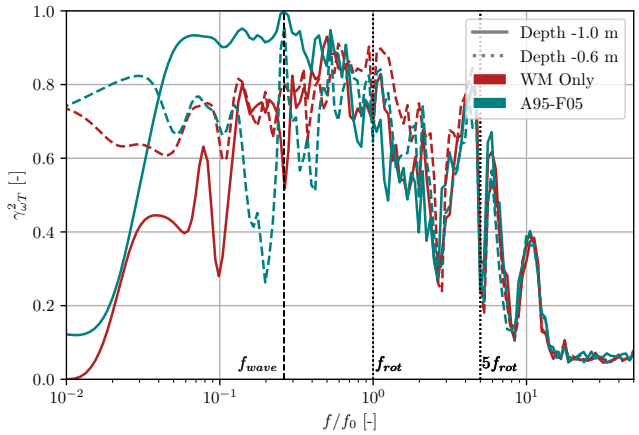

Figure 18: D12 thrust and rotational velocity MSC $\gamma^2_{\omega T}$.

the coherence just in front of the wave frequency is noticeable. Both $\gamma^2_{\omega Q}$ and $\gamma^2_{\omega T}$ are very high for the fifth harmonic of f_{rot} which corresponds to the number of blades. Moreover it strengthens the results of the PSD from fig. 13 and fig. 14. The cut-out frequency is about $6 f_{rot}$ for $\gamma^2_{\omega T}$ and about $12 f_{rot}$ for $\gamma^2_{\omega Q}$. Thus, as in Magallanes Renovables observations, this highlights that the torque is more sensitive to the rotational velocity high frequency variations than the thrust. As for the Magallanes Renovables ATIR turbine, the extinction at f_{rot} of $\gamma^2_{\omega Q}$ is noticed. As previously explained, the reasons behind this phenomenon are unclear. Trials on different stiffness of the control command of the turbine model have been performed and will be analyzed in upcoming works in order to determine an explanation.

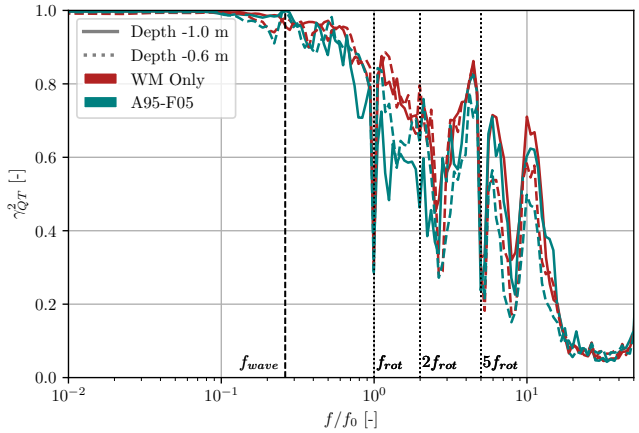

Figure 19: D12 thrust and rotational velocity MSC γ^2_{QT}.

The coherence between torque Q and thrust T is very high till a cut-out frequency of about $10 f_{rot}$. This result is similar to what has been noticed on the ATIR turbine. What is striking and seems to be caused by the turbine geometry and hydrodynamic properties is that Q and T appears to be poorly correlated at the third and fifth harmonics of the rotation frequency, respectively the number of mountings and number of blades.

5 CONCLUSION

This study corroborates the results of the wave effects on turbine performance and blade root loads variation presented in (Dufour et al. 2022). The main following conclusions are drawn:

- Wave changes the turbulence inertial subrange characteristics with an increase of the dissipation rate and a decrease of the injection length scale ;
- Wave creates torque and thrust fluctuations level of the same order as the mean efforts level as seen in PSD, confirmed by the MSC of those efforts with the upstream velocity close to 1 at the wave frequency. A response of torque and thrust is noticed at twice the wave frequency ;
- Both torque and thrust have a response at the rotation angular frequency. Moreover the strongest response, on both PSD and MSC, is seen for both turbines at the number of blades multiplied by the rotation angular frequency ;
- The MSC at z_0 = -1.0 m between upstream velocity and thrust or torque is close to 1 at low frequency and close to 0 at high frequency. On the contrary, the MSC between rotational velocity and thrust or torque is close to 0 at low frequency and close to 1 at high frequency ;
- The MSC at z_0 = -0.6 m between upstream velocity and thrust or torque is the same as the one at z_0 = -1.0 m. However, the MSC at z_0 = -0.6 m between rotational velocity and thrust or torque presents a high level nearly on the whole frequency range.

ACKNOWLEDGEMENTS

This work is co-financed by the European Regional Development Fund (ERDF) through the Interreg Atlantic Area Programme, via the MONITOR project ; and through the Interreg V A France (Channel) England Research and Innovation Programme, via the TIGER project. This work benefits from studies carried out within the framework of H2020 MaRINET2 Round Robin tests and the Interreg 2 Seas MET-CERTIFIED project. This project was partly financially supported by the ERDF, the French government, Ifremer and the region Hauts-de-France in the framework of the project CPER 2015–2020 MARCO.

REFERENCES

Blackmore, T., L. E. Myers, & A. S. Bahaj (2016). Effects of turbulence on tidal turbines: Implications to performance, blade loads, and condition monitoring. *International Journal of Marine Energy 14*, 1 – 26.

Carter, G., C. Knapp, & A. Nuttall (1973). Estimation of the magnitude-squared coherence function via overlapped fast fourier transform processing. *IEEE Transactions on Audio and Electroacoustics 21*(4), 337–344.

Cooley, J. W. & J. W. Tukey (1965). An algorithm for the machine calculation of complex fourier series. *Mathematics of Computation 19*, 297–301.

Dufour, M.-A., B. Gaurier, G. Pinon, G. Germain, J.-V. Facq, M. Togneri, F. Represas, E. Nicolas, & J. Marcille (2022). Comparison of the experimental response of two horizontal axis tidal turbines to wave and current. In *25ème Congrès Français de Mécanique, 25th French Mechanics Congress*.

Furgerot, L., A. Sentchev, P. B. du Bois, G. Lopez, M. Morillon, E. Poizot, Y. Méar, & A.-C. Bennis (2020). One year of measurements in alderney race: preliminary results from database analysis. *Philosophical Transactions of the Royal Society A: Mathematical, Physical and Engineering Sciences 378*(20190625).

Galloway, P. W., L. E. Myers, & A. S. Bahaj (2014). Quantifying wave and yaw effects on a scale tidal stream turbine. *Renewable Energy 63*, 297 – 307.

Gaurier, B., C. Carlier, G. Germain, G. Pinon, & E. Rivoalen (2019). Three tidal turbines in interaction: An experimental study of turbulence intensity effects on wakes and turbine performance. *Renewable Energy*.

Gaurier, B., G. Germain, & G. Pinon (2019). How to correctly measure turbulent upstream flow for marine current turbine performances evaluation? In *Advances in Renewable Energies Offshore: Proceedings of the 3rd International Conference on Renewable Energies Offshore (RENEW 2018), October 8-10, 2018, Lisbon, Portugal. 1st Edition. Carlos Guedes Soares (Ed.). ISBN 978-1-138-58535-5. Modelling tidal currents. pp.23-30 (Taylor & Francis Group)* .

Guo, X., J. Yang, Z. Gao, T. Moan, & H. Lu (2018). The surface wave effects on the performance and the loading of a tidal turbine. *Ocean Engineering 156*, 120 – 134.

Jacquelin, J. (2014). Regressions and integral equations. `https://scikit-guess.readthedocs.io/en/latest/appendices/reei/translation.html`.

Medina, O. D., F. G. Schmitt, R. Calif, G. Germain, & B. Gaurier (2017). Turbulence analysis and multiscale correlations between synchronized flow velocity and marine turbine power production. *Renewable Energy 112*, 314 – 327.

Pishro-Nik, H. (2014). *Introduction to probability, statistics, and random processes*.

Slama, M., G. Pinon, C. El Hadi, M. Togneri, B. Gaurier, G. Germain, J.-V. Facq, J. Nuño, P. Mansilla, E. Nicolas, J. Marcille, & A. Pacheco (2021). Turbine design dependency to turbulence: An experimental study of three scaled tidal turbines. *Ocean Engineering 234*, 109035.

Tennekes, H. & J. L. Lumley (1972, 03). *A First Course in Turbulence*. The MIT Press.

Thiébaut, M., J.-F. Filipot, C. Maisondieu, G. Damblans, R. Duarte, E. Droniou, N. Chaplain, & S. Guillou (2020). A comprehensive assessment of turbulence at a tidal-stream energy site influenced by wind-generated ocean waves. *Energy 191*, 116550.

Togneri, M., E. Buck, A. MacLeod, E. Nicolas, J. Nuño, M. O'Connor, A. Pacheco, G. Pinon, & I. Masters (2019, Sep 1–Sep 6). Multi-model analysis of tidal turbine reliability. In D. Vicinanza (Ed.), *Proceedings of the Thirteenth European Wave and Tidal Energy Conference*, Universitá degli Studi della Campania "Luigi Vanvitelli", Italy. EWTEC. ISSN: 2309-1983.

Welch, P. (1967). The use of fast fourier transform for the estimation of power spectra: A method based on time averaging over short, modified periodograms. *IEEE Transactions on Audio and Electroacoustics 15*(2), 70–73.